New approaches to the linear propagation of acoustic fields

P. Ted Christopher and Kevin J. Parker

Department of Electrical Engineering and Rochester Center for Biomedical Ultrasound,
University of Rochester, Rochester, New York 14627

New algorithms are described that provide insight into linear field propagation and offer significant reductions in computational complexity. The developments presented here include the usage of a recently developed discrete Hankel transform to implement two single step, planar propagation algorithms for baffled, radially symmetric, acoustic pressure or velocity fields; an update on the single step approaches that reduce computational complexity through geometrically determined spatial frequency limitations; and algorithms for extending to multistep propagation. Two equivalent means of introducing arbitrary medium attenuation into the above schemes are presented. Finally, a planar boundary crossing algorithm that accounts for refraction and reflection (but not multiple reflections) is added to one of the multistep propagating algorithms. The resulting algorithm is then used to examine the differences between the corresponding fields of a focused piston source operating in water and in a layered fat/liver (biomedical imaging) medium. The results yield computationally efficient algorithms that can be used for linear propagation of focused or unfocused beams in attenuating, multilayer media, and also provide the basis for a novel nonlinear propagation algorithm.

PACS numbers: 43.20.Bi, 43.20.Hq, 43.20.Tb

INTRODUCTION

The propagation of acoustic fields from realistic sources involves significant effects of diffraction and medium attenuation. The Rayleigh–Sommerfeld diffraction (RSD) formula[1] provides an exact analytical expression for the effects of diffraction on any linear field. For most fields and propagations of interest, though, the analytical solution to this formula is unavailable and the direct numerical evaluation is difficult. This formula is also an expression of Huygen's principle which characterizes diffractive propagation as that of the linear sum of a field's constituent point sources. As such, the diffractive propagation characterized by the Rayleigh–Sommerfeld equation may be viewed as a convolution of the field (usually the source's) with an appropriate point spread function. It is well known that convolution of functions in one domain can be represented as multiplication of the Fourier transforms of the functions, and thus many have used the efficient fast Fourier transform approach to convolutions to calculate diffractive propagation.

One of the first works that addressed the potential of Fourier transforms for the computation of diffractive field propagation was Ratcliffe's.[2] In this work, Ratcliffe used the fact that a two-dimensional Fourier transform of a harmonic field in a plane is equivalent to a decomposition of the field into a sum of harmonic plane waves traveling over a spectrum of angles (this is analogous to the sine wave decomposition implicit in a one dimensional Fourier transform). This equivalent sum of plane waves is referred to as the angular spectrum of the field, and it conceptually allows the diffractive propagation of any harmonic field between two arbitrarily distant, parallel planes to be reduced in complexity to that of plane waves propagating between the same planes. The angular spectrum concept is the transform domain equivalent of Huygen's principle. Ratcliffe covered a wide range of cases to illustrate the application of the angular spectral decomposition to diffraction theory, although the specific application of interest was radio waves in the ionosphere. Optics textbooks such as those by Goodman[3] and Gaskill[1] also discuss this methodology.

In acoustics, the angular spectrum methodology has been utilized by a number of investigators in a variety of applications. Maynard and Williams used it to investigate the possibility of subwavelength resolution acoustic holography[4] and to compute the field from planar radiators.[5] Stepanishen and Benjamin applied the angular spectrum approach to the forward and backward projection of planar acoustic fields.[6] Waag *et al.*[7] reported on a similar investigation except they also explored the important topic of windowing in finite length, discrete operations. The windows investigated included those applied in the spatial domain to the point spread function and those applied in the spatial frequency domain to the analytical transform of the point spread function. Most recently, Shafer and Lewin[8] applied the angular spectrum method to the problem of backpropagation of acoustic fields for the purposes of transducer characterization. These works on acoustic diffraction have been restricted to the use of parallel planes with equispaced, rectangular grids and nonattenuating, homogeneous media.

This paper reports on work further investigating the Fourier transform-based approach to diffractive propagation. Our investigation treats the field propagation of planar, baffled, radially symmetric acoustic sources, though the general principles expounded in the paper are applicable to nonradially symmetric, planar sources as well. The constraint of radial symmetry allows our computational efforts to be greatly simplified by utilizing a recently developed, discrete Hankel transform (DHT) algorithm. After briefly

presenting this DHT algorithm, we will then present radial fields computed for a baffled, uniform amplitude, piston source using two different transform based, single step, propagation algorithms and discuss the serious shortcomings revealed in the traditional angular spectrum-based algorithm. Next using a geometric spatial frequency relation or "ray theory" approach, and improved angular spectrum algorithm is explored. Then we present two incremental, multistep propagation algorithms based on the single step propagation algorithms. The axial pressure and normal velocity fields of the same uniform amplitude piston source are computed using these algorithms and compared with an analytical pressure solution. Next, equivalent means of introducing medium absorption in the spatial and transform domains are shown. Finally, we present an algorithm for field propagation through multiple, parallel layers of fluid medium and utilize it to consider the differences between the corresponding focused fields in water and a layered fat/liver (biomedical imaging) medium. This multilayer algorithm does not consider multiple reflections and thus is not appropriate for some applications.

Together, the results demonstrate a computationally efficient means for propagating radially symmetric fields through a range of conditions germane to medical ultrasound imaging, underwater acoustics, and other applications. The general treatment of the angular spectrum propagation scheme provides useful insights into diffractive problems in linear acoustics. The methodologies also serve as the starting point for the treatment of diffractive wave propagation in a nonlinear medium, which is covered in a companion paper.

I. THE DISCRETE HANKEL TRANSFORM

Many applications in ultrasound and acoustics use sources that are radially symmetric. To greatly reduce the temporal and spatial computational requirements of the propagation of fields from such radially symmetric sources, we have chosen to use a discrete Hankel transform (DHT) instead of the traditional two dimensional discrete Fourier transform. Even when the fields of interest are not radially symmetric the DHT may present significant computational savings in simplifying the transforming of the radially symmetric point spread function.

The discrete Hankel transform algorithm selected was recently developed by H. Fisk Johnson. Johnson's paper[9] provides evidence that the algorithm is a significant improvement over other existing DHT algorithms, especially in applications involving inverse transforms such as in convolutions. Thus, the algorithm appears well suited to diffractive field propagation problems.

Johnson's algorithm gives output in the Fourier domain in terms of radians per unit length. We have chosen to convert the algorithm to produce output in cycles per unit length. The resulting pair of discrete Hankel transform equations for a radial function $f(r)$ (which describes the radius of a radially symmetric, two dimensional function) and the corresponding Fourier transform domain radial function $F(R)$ is

$$f(i) = \frac{1}{2\pi T^2} \sum_{m=1}^{N-1} Y(i,m)F(m), \tag{1}$$

$$F(m) = \frac{2\pi T^2}{j_N^2} \sum_{i=1}^{N-1} Y(m,i)f(i), \tag{2}$$

where j_N is the Nth zero of the Bessel function $J_0(x)$ and

$$f(i) = f(j_i T/j_N),$$

$$F(m) = F(j_m/2\pi T),$$

$$Y(i,m) = 2J_0(j_i j_m/j_N)/J_1^2(j_m).$$

T is the transform extent in real space and $N-1$ is the number of discrete samples. Note that the resulting $N-1$ points in the real and transform domain are located radially at points determined by the zeros of $J_0(x)$. Thus the input and output to the transforms are not equispaced values as with Fourier transforms. Interpolation formulas are provided in Johnson's paper, though, which allow the Bessel-spaced output points from either transform to be converted to any others in the output range desired. We have used these interpolation formulas to extend the above transforms to include an output value at $r = 0$ in real space (corresponding in our application to the on-axis point) and at $R = 0$ in Fourier space (corresponding to the dc or zero frequency point).

Our implementation of the Johnson DHT algorithm uses Unix math library routines to calculate the Bessel functions $J_0(x)$ and $J_1(x)$. To acquire the necessary zeros of $J_0(x)$ the asymptotic formula from p. xxxvii of the British Association for the Advancement of Science, Bessel Functions, Part II (1952) was used (a shorter version of this formula is Eq. 9.5.12 on p. 371 of Abramowitz and Stegun and several other references are also listed here). These zeros were in turn used as initial values in a Newton's method algorithm to insure accuracy. To minimize the recalculation of necessary transform constants, a $Y(i,m)$ table was computed and stored at the beginning of any program utilizing the DHT. Alternatively, if an application involves long term usage of DHT's with the same N and T then the corresponding $Y(i,m)$ table could be computed once and saved for future program runs.

For a given N complex radial samples over T radial extent, Johnson's DHT algorithm requires the computation of $2 \times N^2$ real multiplications and real additions [after computing the $Y(i,m)$ table]. Assuming N is a power of 2, a standard complex, 2-D FFT routine would require $(2N)^2 \log_2(2N)$ complex multiplications and $2 \times (2N)^2 \log_2(2N)$ complex additions. Assuming on the other hand that the function's x and y complex symmetry are fully utilized, then the minimal 2-D, FFT implementation requires $N^2 \log_2 N$ real multiplications and $2 \times N^2 \log_2 N$ real additions. Assuming that a real multiplication takes the same time as a real addition then the DHT's complexity can be written as $4 \times N^2$ real operations, the standard 2-D FFT's complexity as $10 \times (2N)^2 \log_2(2N)$ real operations ("10" here accounts for the conversion of complex operations to real operations), while that of the optimized 2-D FFT implementation can be written as $3 \times N^2 \log_2 N$ real operations. The spatial complexity of the input to the DHT algorithm is $N-1$ (a radius of real or transform data), that of the corresponding standard 2-D FFT is $(2N)^2$ (a full square grid

enclosing the radial real or transform data), and that of the minimal 2-D FFT is N^2 (a quadrant of real or transform data).

On the authors' Digital VAXstation II/GPX, a DHT with $N = 256$ requires 4 s of CPU time, with $N = 512$ the DHT requires 13 s. The CPU time used to compute the corresponding $Y(i,m)$ tables was 42 and 172 s, respectively. Using the above approximate expressions for the complexities and the recorded CPU execution times for the DHT algorithm, estimates can be obtained for the CPU execution times of a standard and an optimal 2-D FFT routine executing on our model of computer. For $N = 256$ the predicted CPU times are 450 and 30 s, respectively. For $N = 512$ the predicted times are 1300 and 88 s, respectively. One additional advantage of the Johnson's DHT is that it has no sample length constraints—power of 2 or otherwise.

II. TWO APPROACHES TO SINGLE-STEP PROPAGATION

Before proceeding to describe and utilize two practical discrete transform-based propagation algorithms, we first present the analytically derived expression for the radial pressure field in a plane z_1 due to a harmonic point pressure source in a parallel plane z_0,[7]

$$h(z,r) = -\frac{1}{2\pi}\frac{z}{d^2}\left(j2\pi\frac{f}{c} - \frac{1}{d}\right)e^{jkd},$$

where

$$z = z_1 - z_0, \quad d = \sqrt{r^2 + z^2}, \quad k = 2\pi(f/c). \quad (3)$$

This expression also gives the radial normal velocity field in the plane z_1 due to a harmonic normal velocity point source in the parallel plane z_0 (this result can be easily derived from the Rayleigh integral which relates pressure in a plane to the planar, normal velocity profile of the source). For a 3-MHz point source in water ($c = 1500$ m/s), the magnitude and phase of $h(z,r)$ as a function of r is shown for two values of z in Fig. 1(a).

The analytical Hankel transform of $h(z,r)$ is

$$H(z,R) = \begin{cases} \exp\left[j2\pi z\sqrt{(f/c)^2 - R^2}\right], & |R| \leqslant f/c, \\ \exp\left[-2\pi z\sqrt{R^2 - (f/c)^2}\right], & |R| > f/c. \end{cases} \quad (4)$$

The magnitude and phase of $H(z,R)$ corresponding to the above described 3 MHz $h(z,r)$ is shown as a function of R (spatial frequency in cycles per centimeter), again for the same values of z in Fig. 1(b). $H(z,R)$ is the propagation function for the angular spectrum method and as such, the value of $H(z,R)$ could be directly calculated from geometric considerations. The basic geometric relation is

$$R = (f/c)\sin\theta, \quad (5)$$

where θ is the complex angle between a plane and the propagating plane wave ($\theta = 0°$ when the plane wave is normal to the plane), which together correspond to a spatial frequency of R in the plane (due to the plane wave). The angular spectrum analogy offers a good conceptual understanding of the two distinct regions of $H(z,R)$. For a given z, the radial region for $|R| \leqslant f/c$ corresponds to the phase only propagation factors for the source's plane wave components. These plane

wave components have directions given by $0° \leqslant \theta \leqslant 90°$ in expression (5). Note that as $|R| \rightarrow f/c$ the derivative of $H(z,R)$ with respect to R goes to infinity. The remaining region for which $|R| > f/c$ corresponds to the exponentially decaying real propagation factors for the source's evanescent wave components (here θ is imaginary). Note the exponentially decaying tail is only visible in the $z = 0.05$-cm (1-λ) figure.

In order to apply discrete transforms to single-step propagation of fields, sampling must be performed across some finite extent of the source and propagation functions. Two approaches, with different consequences, can be taken here. One of these algorithms directly samples $h(z,r)$ and we shall call this the spatially sampled convolution (SSC) algorithm. The other directly samples $H(z,R)$ and we shall call this the frequency sampled convolution (FSC) algorithm. Though the analytical analogs of these algorithms are equivalent, significant differences exist between these two algorithms as implemented due to the finite length discrete transform operations used. We shall first present the SSC algorithm. Assume that the finite, complex normal velocity field of some harmonic source is known or can be well approximated in some initial plane z_0 and is desired in some subsequent plane z_1. Call the complex function describing this initial planar field $s(z_0,r)$. The SSC algorithm then consists of the following steps:

(1) Select a radius, r_d, greater than the source radius a over which correct field propagation results are desired. This determines the minimum transform extent as $T \geqslant r_d + a$.

(2) Select a spatial sampling rate, ψ, which exceeds the Nyquist requirements of the highest expected spatial frequency emitted from the source. We often use $4 \times f/c$ as this ensures finely sampled output and the inclusion of any significant evanescent waves. The number of radial samples is then $N = \psi \times T$.

(3) Using the above specified N and T, compute the specified samples of function $s(z_0,r)$. Call these complex values $s_d(i)$, $i = 1,...,N - 1$. Compute the DHT of these s_d values. Call the complex transform output values $S_d(m)$, $m = 1,...,N - 1$.

(4) Again using the same N and T, compute the specified samples of $h(z_1 - z_0,r)$, where $z_1 - z_0$ is the desired propagation distance. Call these values $h_d(i)$, $i = 1,...,N - 1$. Compute the DHT of these h_d values. Call these complex transform output values $H_d(m)$, $m = 1,...,N - 1$.

(5) Compute the complex product $S_d(m) \times H_d(m)$, $m = 1,...,N - 1$. Now compute the inverse DHT of this product to obtain the desired complex field result. Call these normal velocity field results $u_d(z_1,i)$, $i = 1,...,N - 1$.

(6) Now the u_d values can be examined as real and imaginary components, or by computing their magnitude and phase. Note that the field samples describing $r_d < r < T$ contain "wraparound error," from the transform-based convolution.

The SSC algorithm corresponds to a direct application of the fact that convolution in the spatial domain corresponds to multiplication in the transform domain, with the understanding that all discrete transform operations are im-

plicitly periodic. The other algorithm that we consider in this section, the (spatial) frequency sampled convolution (FSC) algorithm is a computational simplification of the SSC. The two algorithms differ only in step 4 where the FSC algorithm has the abbreviated step:

(4′) Using the previously determined N and T, directly sample $H(z_1 - z_0, R)$ to obtain $\hat{H}_d(m)$ $m = 1,...,N - 1$ (The inverse DHT of this shall be written $\hat{h}_d(i)$, $i = 1,...,N - 1$). Now use these values as the H_d values were used in the SSC algorithm. The final results obtained using the FSC algorithm shall be written $\hat{u}_d(z_1,i)$, $i = 1,...,N - 1$.

The approach of the FSC algorithm is consistent with what in digital signal processing is referred to as frequency sampling. The consequences of this short cut will be noted in the propagation example next.

In both of these algorithms, pressure results (instead of normal velocity results) can be obtained by replacing h or H with the corresponding normal velocity to pressure propagation function (h_{up} or H_{up},[5] respectively). Since most of the commonly considered sources have a finite extent normal velocity profile, most of our examples will involve the propagation of a normal velocity source profile. A later section will briefly consider the propagation of a source's pressure profile.

Consider a 3-MHz, uniform amplitude, unfocused piston transducer of radius 1 cm and initial acoustic peak intensity of 0.1 W/cm^2. The acoustic medium is water with $c = 1500$ m/s and no acoustic attenuation is included here. Following the above listed algorithm steps a radial extent of correctness of $r_d = 3$ cm is desired, this determines a transform extent of $T = 4$ cm. The formula $4 \times f/c$ gives a sampling rate ψ of 80 samples/cm. Together ψ and T determine a
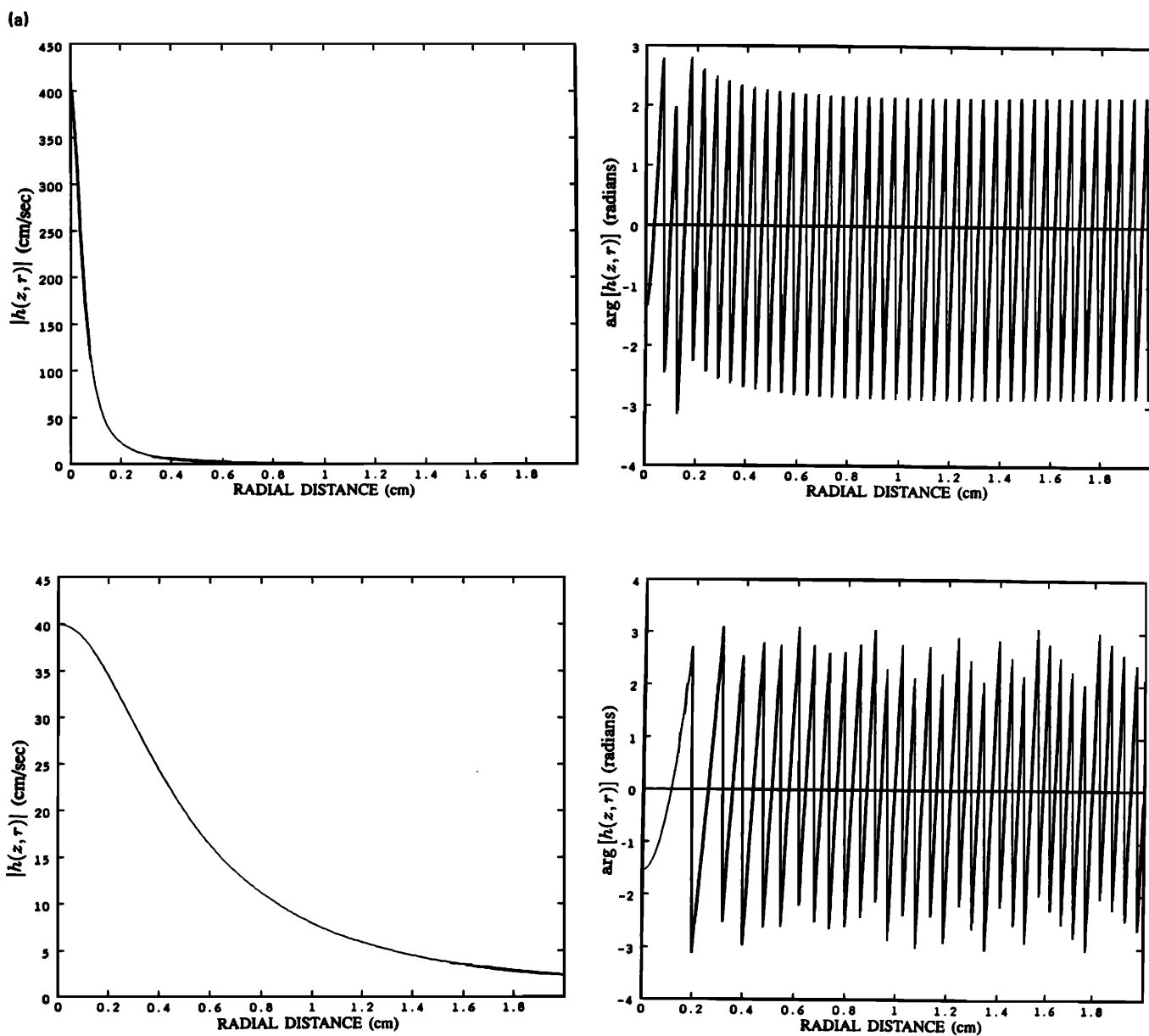
(a)

FIG. 1. (a) The point source function $h(z,r)$ for a 3-MHz normal velocity point source at $z = 1\lambda$ (top) and 10λ (bottom). Magnitude (left side) and phase (right side) are shown for both distances. (b) The corresponding $H(z,R)$ plots.
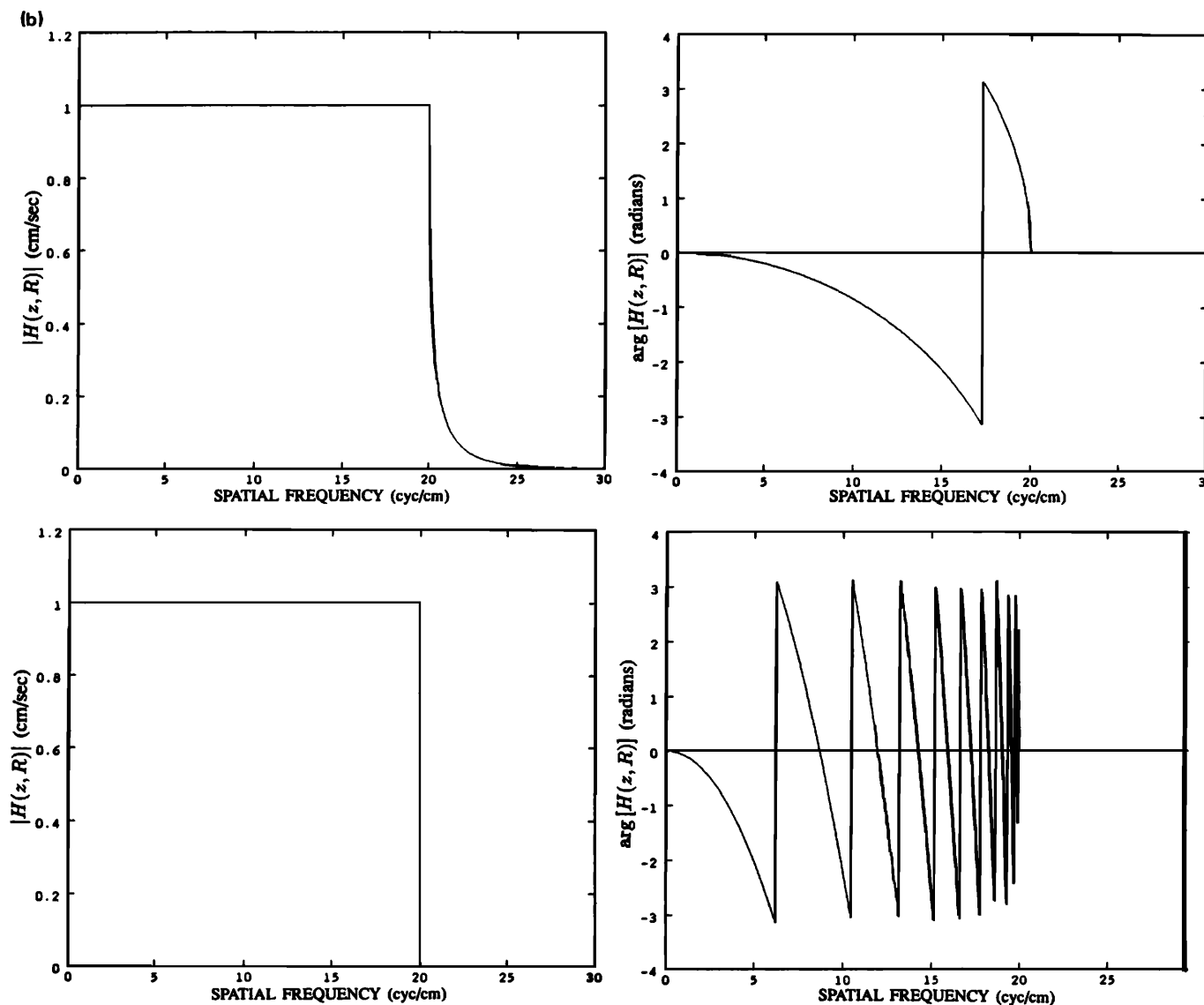
P. T. Christopher and K. J. Parker: Linear propagation

(b)

FIG. 1. (*Continued.*)

total sample count of $N = 320$. The resulting radial normal velocity amplitude profile of $s_d(i)$ is shown in Fig. 2(a). The DHT of this, $S_d(m)$, is shown in Fig. 2(b). In Fig. 2 (c) and (d) are shown overlays of h_d and $\hat{h}_d$ and their DHT's H_d and $\hat{H}_d$ for $\Delta z = 0.05$ cm (1 wavelength or λ). In Fig. 2(c) h_d is the smooth curve, while in (d) its DHT, H_d, is the curve with the visible Gibbs phenomenon wiggle. Figure 2(e) and (f) are the same format as 2(c) and (d) except here $\Delta z = 20$ cm (400 wavelengths) which equals a^2/λ the approximate distance from the source to the last axial maximum.

The radial normal velocity field results obtained by propagating the 3-MHz, unfocused piston transducer field out 1 and 400 wavelengths axial distance using the SSC and FSC algorithms are shown in Fig. 2(g)–(j). Figure 2(g) and (h) are linear and log scaled overlays of the magnitude of u_d (0.05 cm,i) and $\hat{u}_d$ (0.05 cm,i), respectively (phase overlays are not used here as they reveal the same differences, only in a much more subtle fashion). The only significant difference between these two results is revealed in the log scaled figure, where $|u_d|$ is smooth out to 3 cm ($= r_d$) and thereafter is

predictably bad due to convolutional wraparound error, $|\hat{u}_d|$ on the other hand visibly starts to deviate from a convolutionally correct result at about 2 cm. A more striking difference in the results of these two algorithms is revealed in comparing $|u_d$ (20 cm,i)$|$ and $|\hat{u}_d$ (20 cm,i)$|$. Figure 2(i) is a linear plot of $|u_d|$, while Fig. 2(j) is a linear plot of $|\hat{u}_d|$. The results of the FSC algorithm as depicted in the curve of $|\hat{u}_d|$ are very poor at all radial distances.

The differences just observed can easily be illuminated by considering the well established principles of discrete convolution.[10] The SSC algorithm by using a sufficiently large sampling rate, ψ, directly sampling the spatial functions $s(z_0,r)$ and $h(z,r)$; and then transforming, multiplying the results, and inverse transforming the product, correctly implements the discrete, circular version of the (Fourier) convolution theorem. Thus in the case where $\Delta z = 20$ cm, $s(z_0,r)$ and $h(20$ cm,$r)$ are very accurately convolved to a radial extent of 3 cm (r_d) by discretely convolving $s_d(i)$ and $h_d(i)$ as described in the SSC algorithm example. The only source of errors in the resultant u_d (20 cm,i) values (where $r = j_i T/j_N < 3$ cm) should be attributable to finite sampling
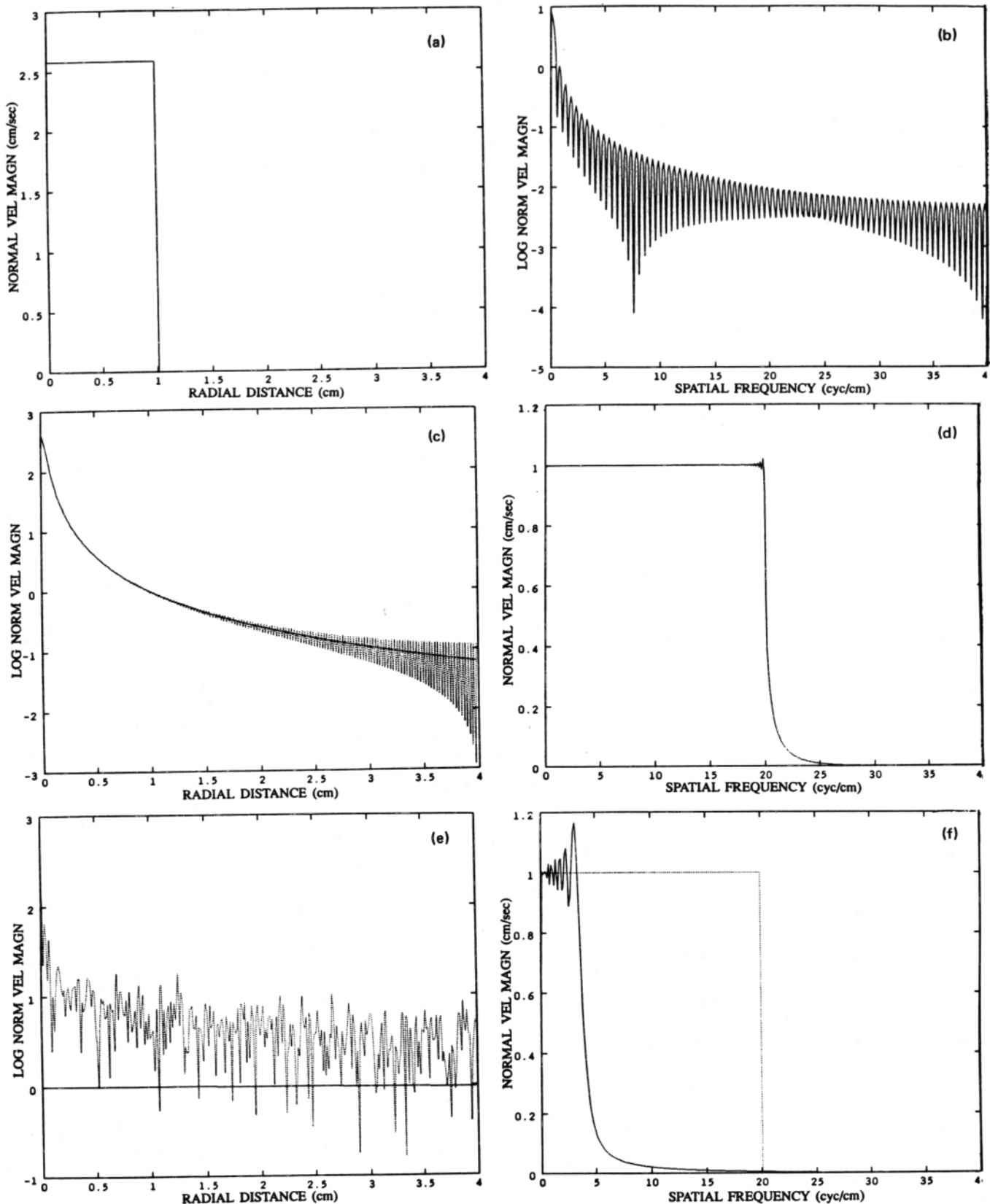
FIG. 2. SSC- and FSC-based propagation of a 3-MHz uniform piston source of radius 1 cm. The medium is water and no attenuation is included in the propagations. The number of discrete field samples N is 320 and the transform extent T is 4 cm. (a) The magnitude of the acoustic normal velocity profile of the piston source ($|s_d(i)|$). (b) The magnitude of the DHT of the source profile ($|S_d(m)|$). (c) Overlay of $|h_d(i)|$ and $|\hat{h}_d(i)|$ for $\Delta z = 0.05$ cm (1λ). $|h_d(i)|$ is the solid curve (all subsequent SSC–FSC overlays will use the format SSC solid curve, FSC dotted curve). (d) Overlay of the corresponding $|H_d(m)|$ and $|\hat{H}_d(m)|$. The $|H_d(m)|$ curve has a little visible Gibbs ringing. Note the evanescent tails extending beyond f/c (20 cycles/cm). (e) and (f) are identical in content and format to (c) and (d), respectively, except here $\Delta z = 20$ cm. Note the log scale in (e). (g) and (h) are linear and log scaled overlays of $|u_d(0.05$ cm,$i)|$ and $|\hat{u}_d(0.05$ cm,$i)|$, respectively. The only significant difference between these curves is revealed in the log scaled plot where $|u_d(0.05$ cm,$i)|$ stays smooth (and correct) out to 3 cm. (i) is a linear plot of $|u_d(20$ cm,$i)|$ and (j) is a linear plot of $|\hat{u}_d(20$ cm,$i)|$. Note the miserable result in (j) due to the FSC algorithm's uncorrected wraparound error.
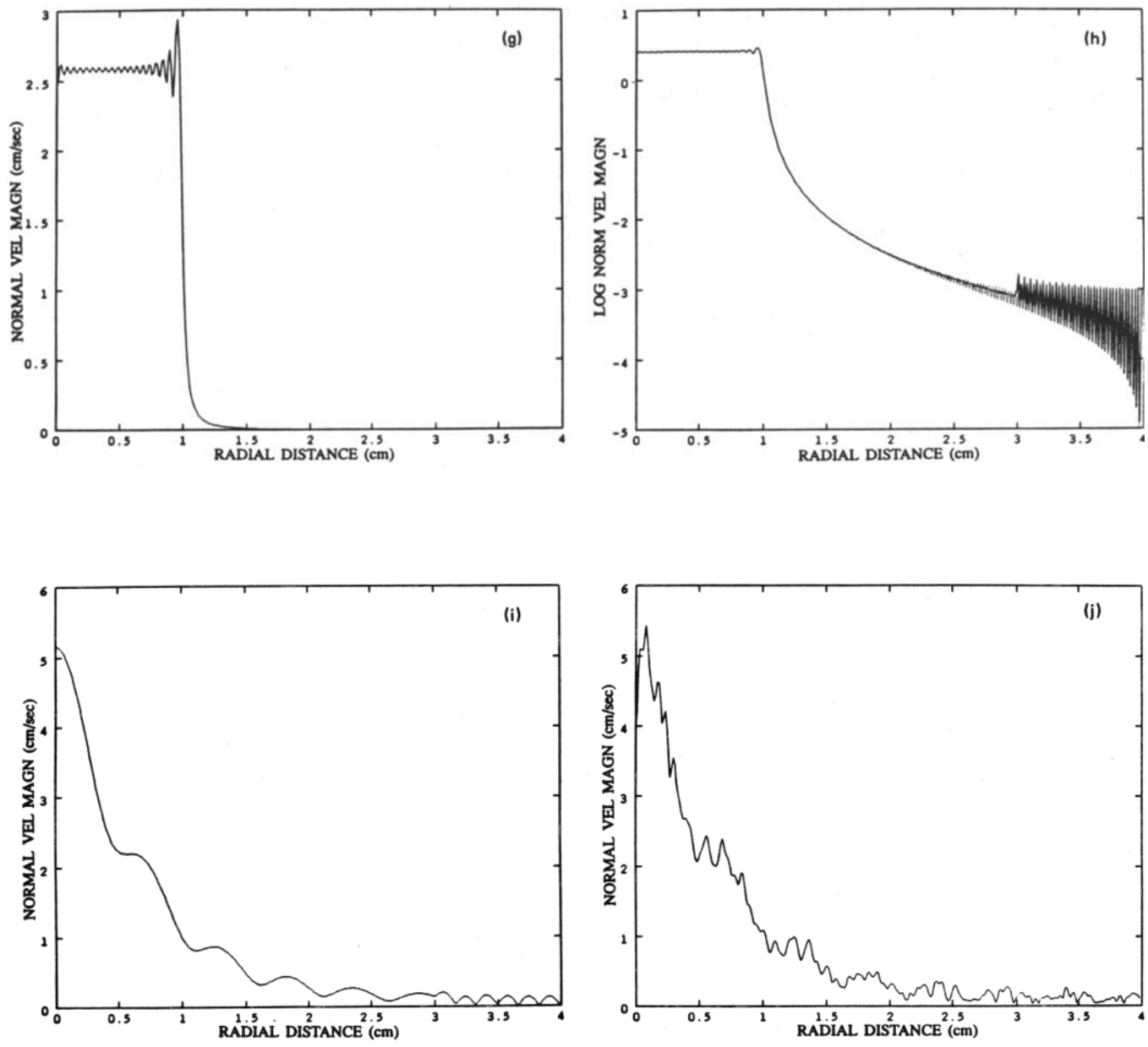
FIG. 2. (*Continued.*)

(since a finite extent, continuous function like the source function has an infinite extent, continuous spatial frequency content) and inaccuracies in Johnson's DHT itself. The small errors due to truncating real numbers to double precision or approximately 16 decimal places of accuracy, can be safely ignored here (this is probably also true for single precision). To examine the possible size of the DHT and sampling errors the transform extent and sampling rate were increased. This should have reduced the sampling errors by increasing the spatial frequency resolution and ceiling, as well as reduced the DHT inaccuracies.[9] With the SSC algorithm though, the u_d results show very small improvements only in the extreme near field (0–20 λ, see the multistep section.). Thus it appears that the predicted acoustic normal velocity field of the piston source is in very good agreement with the best possible prediction, an analytical solution based on Huygen's principle.

The implementation of discrete convolution by the FSC algorithm is markedly different. Whereas the SSC algorithm discretely convolves the s_d and h_d samples, the FSC algorithm is instead equivalent to a discrete convolution of the s_d and $\hat{h}_d$ samples. The $\hat{h}_d$ samples were obtained by directly sampling $H(z,R)$, the analytical Hankel transform of the infinite extent $h(z,r)$ function, and then performing a (finite extent) inverse DHT on these samples. Thus the $\hat{h}_d$ samples correspond to samples of the infinite h function which has been infinitely wrapped around to produce a finite function of radial extent T. Such a wrapped around version of h could be physically approximated by propagating the field of an appropriate normal velocity (or pressure) point source

P. T. Christopher and K. J. Parker: Linear propagation

down a cylindrical reflecting tube of radius T. When z is small the resulting wraparound error can be very small as shown by the close correspondence between the h_d and $\hat{h}_d$ sample curves plotted in Fig. 2(c). For larger values of z these errors can be overwhelming as evidenced in the curves of Fig. 2(e). Also note the corresponding differences in the transform domain curves of Fig. 2(d) and (f). Thus, it is not surprising that large errors can appear in the output of the FSC algorithm.

In spite of these problems with the FSC algorithm, it appears to be the most widely used approach to the propagation of diffractive acoustic fields, perhaps because of its conceptual similarity to the analytical angular spectrum methodology. However, the perils of "frequency domain sampling" of a continuous transform function are well known in digital signal processing, and we have shown that the FSC approach is only numerically convergent in the case where $z \to 0$ (or equivalently $T \to \infty$). In contrast the SSC algorithm is convergent for any Δz propagation (with reasonable sampling rates though, the SSC algorithm fails for propagation distances $\ll \lambda$ due to limited sampling of the significant portion of the function $h(z,r)$, which approaches a delta function when $z \to 0$). We thus argue that the SSC algorithm should be the first choice (over the FSC algorithm) for plane-to-plane, linear diffractive propagation.

III. A RAY THEORY TRUNCATION FOR THE FSC ALGORITHM

The FSC algorithm can be greatly improved by modifying it with a ray theory interpretation of the h–H transform pair. Since the field of a point source at distances greater than λ can be very well described by ray theory (which only neglects the point source's evanescent waves), it thus follows that this same theory well describes the $h(z,r)$ function for $\sqrt{z^2 + r^2} > \lambda$. Consider the field of a harmonic normal velocity (or pressure) point source as depicted in Fig. 3(a). In particular, consider the radial spatial frequency (or radial derivative of the phase) of the resultant field at some point p_i in the plane P. Given the geometry depicted in Fig. 3(a) a ray theory interpretation of the field would suggest that the radial spatial frequency, η_{r_i}, of the field in plane P at point p_i should be given by the expression

$$\eta_{r_i} = (f/c) \sin \theta_{r_i}, \text{ cycles/unit length.} \tag{6}$$

As pictured, θ_{r_i} is the angle between the ray connecting a point at radial distance r_i and the point source, and a ray normal to P at the same point. In (6) the spatial frequency increases monotonically from 0 to f/c as r_i goes from 0 to ∞. Note that this expression is the real, spatial domain version of that given in expression (5) [i.e., the field in the vicinity of p_i approximates a plane wave with direction θ_{r_i} and spatial frequency R given by (5)]. Expression (6) was first presented and utilized in Waag et al.,[7] in this and the following section we attempt to further explore and elaborate on the utility of applying this result to the FSC algorithm.

Figure 3(b) and (c) show the results of tests on the above ray theory relation at $\Delta z = 1\lambda$ and 10λ, respectively. The solid lines were computed using the above approximate
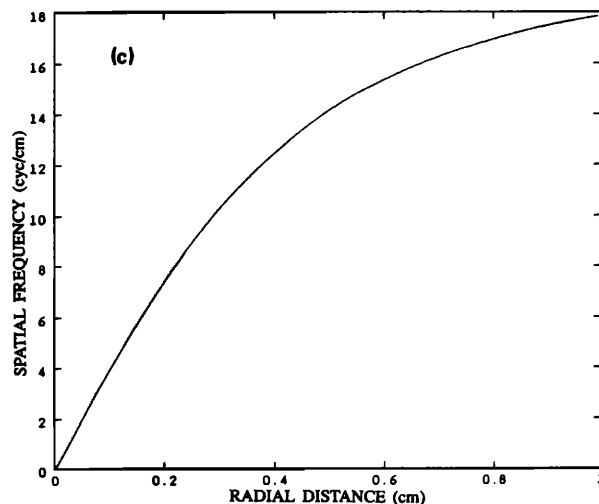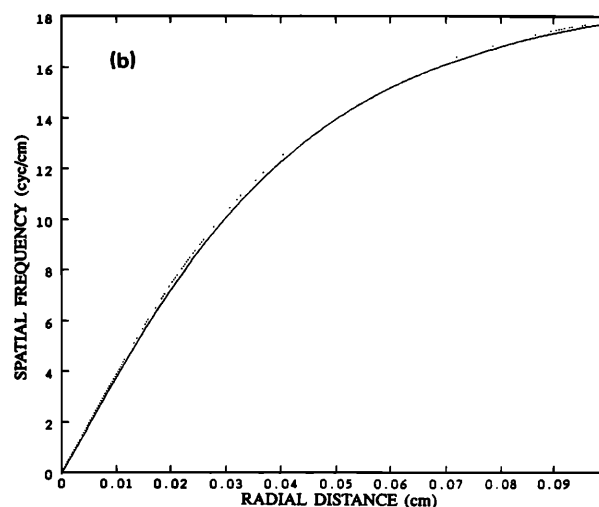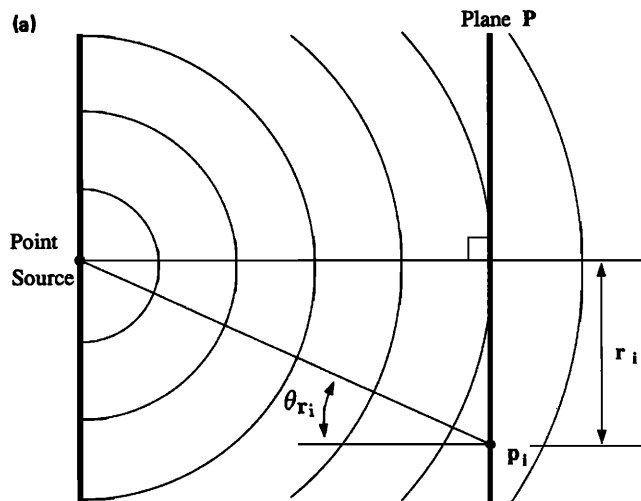

FIG. 3. (a) Geometry for the ray theory interpretation of $h(z,r)$. (b) Ray theory-derived radial spatial frequency overlayed with the derivative of $h(z,r)$'s phase at $\Delta z = 1 \lambda$. Ray theory is the lower curve (evanescent waves, neglected by ray theory, account for the difference). (c) Same overlay this time at $\Delta z = 10 \lambda$.

relation for a 3-MHz normal velocity point source in water. The dotted lines were derived from the computed rate of phase change at the corresponding (actual field) $h_d(i)$ samples ($N = 200$, $T = 5$ cm). To obtain an estimate of the spatial frequency at the $h_d(i)$ samples, the forward difference method of calculating the derivative was used. The spatial frequency values obtained from the approximate ray theory relation and those computed directly from $h(z,r)$ show small differences at $\Delta z = 1\lambda$ due to the presence of evanescent waves, but then quickly converge as the evanescent waves fade.

For the field of some harmonic, finite (acoustic normal velocity profile) emitter, expression (5) can be combined with Huygen's principle to estimate the magnitude of the maximum spatial frequency contribution of the emitter's constituent point sources to a point in the field. Using this, and again neglecting evanescent waves, a reduced minimum spatial sampling rate can be determined. Call the angle between the normal ray at a point p_1 in a plane and the ray passing through the same point and also the most distant point source contributor in the emitter plane, θ_1^{max}. This is depicted in Fig. 4(a) (along with an additional point p_2). Substituting θ_1^{max} into (5) gives a reduced (radial) spatial sampling rate, ψ_1^{max}, required to meet the Nyquist criteria in

sampling $h(z,r)$ for the given Δz, in the radial range from $r = 0$ to $r = r_i + a$. This reduced sampling rate can then be used directly to update the SSC algorithm's sampling of $h(z,r)$, or indirectly to update FSC's sampling of $H(z,R)$. Figure 4(b) shows the truncated $H(z,R)$ functions associated with p_1 (and θ_1^{max}) and p_2 (and θ_2^{max}). The spatial frequency relation not only allows for a reduction in the computational requirements of the two algorithms, but more importantly it greatly reduces the wraparound errors present in the FSC algorithm.

The idea of limiting the maximum spatial frequency used in computation by ray theory or geometric considerations leads to a simple truncation of the $\hat{H}_d$ function and we call this approach the ray theory-updated, FSC algorithm (RFSC). Applying RFSC to the previously described 3-MHz uniform piston field is illuminating. Consider the radial field at the Rayleigh distance of $z = 20$ cm. Assuming that good field results are desired out to a radial distance of $r_d = 5$ cm, then $a = 1$ cm implies that the sampling rate $\psi_{r_i}^{max}$ must be greater than or equal to $2 \times (f/c)\sin(\theta_{r_d})$ where $\theta_{r_d}^{max} = \tan^{-1}[(5 + 1)/20] = 16.69°$. After choosing $T = 10$ cm this implies $N = 120$. Using these in the RFSC algorithm gives the $|\hat{H}_d|$ and $|\hat{h}_d|$ samples shown in Fig. 5(a) and (b). Also shown in Fig. 5(b) is the corresponding $|h_d|$ samples [note the vast improvement in the agreement of these curves compared to Fig. 2(e)]. In Fig. 5(c) is the resulting output radial field $|\hat{u}_d|$ values from the RFSC algorithm as well as $|u_d|$ values from the SSC algorithm ($N = 500$, $T = 10$ cm, and $r_d = 9$ cm). Note the good agreement between the curves out to about 5 cm and the subsequent smooth divergence of the $|\hat{u}_d|$ dotted curve (as predicted by ray theory).

The ray theory relation of Eq. (6) offers a reduced minimum sampling rate to all of the propagation algorithms— though this relation should be superseded by the sampling rate requirement in the emitter plane, if this is larger. Alternatively, if a higher spatial sampling rate is desired or required, (6) allows the frequency domain sampling FSC algorithm to accurately mimic the (correct) spatial domain sampling of the SSC algorithm. This can be accomplished by simply limiting the FSC's sampling of $H(z,R)$ to those values of $R < (f/c)\sin(\theta_{r_d}^{max})$. Thus, the validity of ray theory in describing a point source's field provides for a unique, h–H transform pair, with which the convolutionally necessary windowing in the spatial domain can instead by accurately and easily accomplished in the frequency domain. To ensure good results though, a relatively large T (greater than 5 or 10 source radii) should be used to obtain adequate spatial frequency domain resolution, or equivalently, sufficiently many plane waves to represent the field accurately. Even with this additional requirement, the RFSC method has much to offer in some applications as discussed in the next section.

(a)

Piston
Source
(rad.=a)

θ_1^{max} θ_2^{max}

a

r_i

P_1 P_2

(b)

NORMAL VEL MAGN (cm/sec)

1.2

1

0.8

0.6

0.4

0.2

0

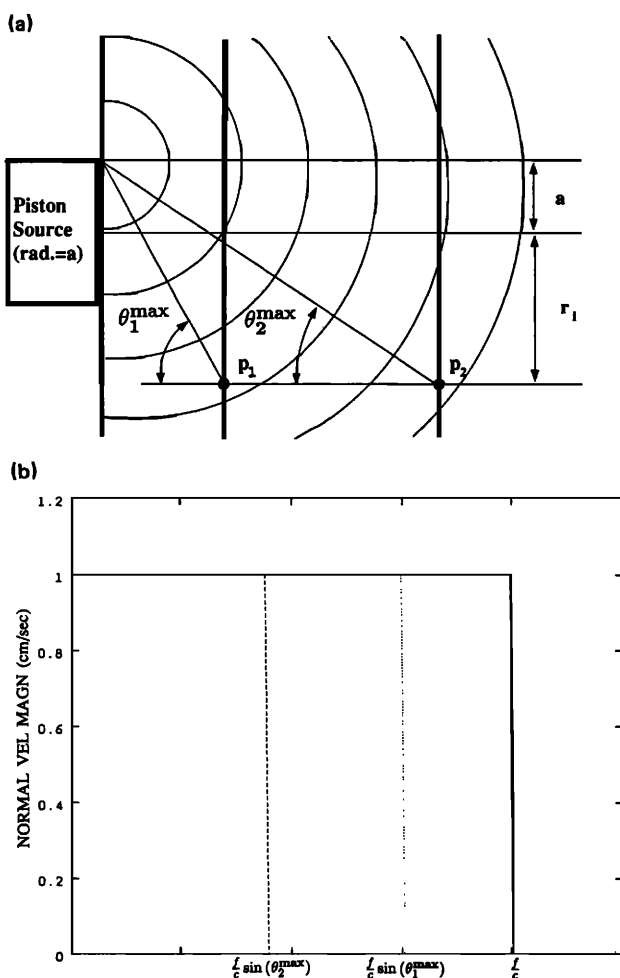$\frac{f}{c}\sin(\theta_2^{max})$ $\frac{f}{c}\sin(\theta_1^{max})$ $\frac{f}{c}$

FIG. 4. (a) Geometry for the ray theory RFSC propagation step. (b) The associated, truncated $H(z,R)$ functions. The truncation points are determined by the geometry of 4(a) and the spatial frequency relation (5).

IV. EXTENSION TO MULTISTEP PROPAGATION

The SSC and RFSC single step, plane-to-plane, propagation algorithms can be extended to multistep algorithms. If the field of a planar source is desired in a sequence of
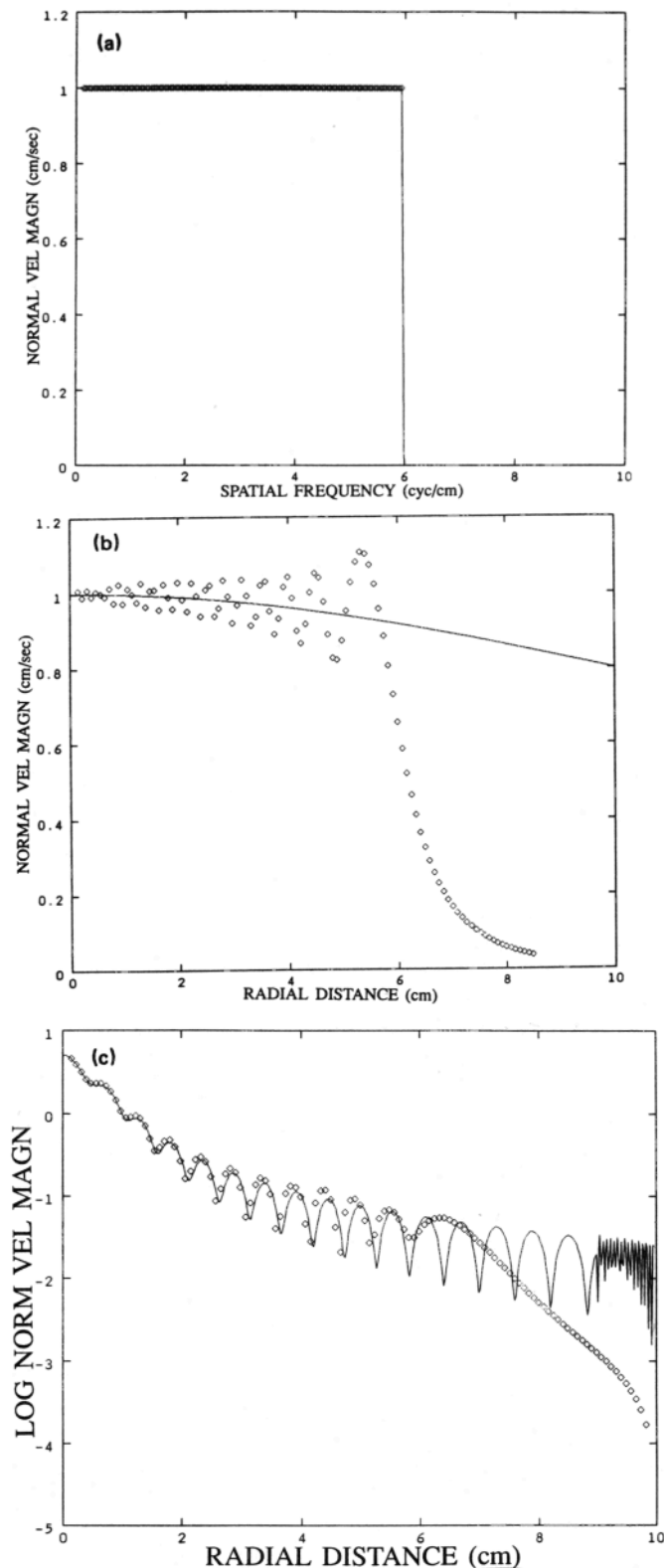
FIG. 5. Uniform piston (same case as Fig. 2) example of the RFSC step at the Rayleigh distance of 20 cm from the transducer. (a) $|\hat{H}_d(m)|$ for the RFSC step. Note that $f/c = 20$ cycles/cm, so $\hat{H}_d(m)$ propagates only 1/3 of the spatial frequencies contained in the full $H(z,R)$ function. (b) RFSC's $|\hat{h}_d(i)|$ ($\Diamond$'s) and SSC's $|h_d(i)|$ (solid curve) overlayed. Note the rough agreement to $r = 6$ cm in spite of RFSC's Gibbs ringing (compare to Fig. 2(e)'s *log scaled* overlay). (c) Rayleigh distance RFSC output $|\hat{u}_d(i)|$ ($\Diamond$'s) overlayed with SSC output $|u_d(i)|$ (solid curve). They agree well with the SSC curve out to the desired $r = 5$ cm. The small shift in the radial node positions visible between the two results is due to the different source radii implicit in the different discretizations of the actual 1-cm source. (This problem can be corrected by updating T appropriately).

parallel planes then the SSC or RFSC step could be repeated for each of these planes. Since the only plane in which the normal velocity field is of finite extent is the source plane, each SSC or RFSC iteration *must* begin there—otherwise the iterative propagation of truncated infinite fields quickly causes large errors. The source plane transform should be computed once and then repetitively used for each SSC or RFSC iteration.

Figure 6(a)–(d) display the results of testing the SSC-based multistep algorithm against the analytical axial pressure amplitude expression for a uniform piston source.[11] The analytical axial amplitude expression used was

$$|p(z,0)| = 2\rho c U_0 |\sin\{\tfrac{1}{2}kz[\sqrt{1+(a/z)^2}-1]\}|, \quad (7)$$

where ρ is the medium density and U_0 is the magnitude of the source's normal velocity. The source and medium parameters are the same as before for the 3 MHz, unfocused piston source. The agreement between the SSC algorithm and theory is excellent in the near and far field as displayed in Fig. 6(a) and (b). Figure 6(c) reveals small differences in the extreme near field (0–$20\,\lambda$). The radial sampling rate used for these results (a)–(c) was $4 \times f/c$ ($2 \times$ Nyquist rate). By increasing the radial sampling rate, the edge discontinuity of the source can be better represented, and thus the near field can be more accurately computed. Figure 6(d) shows the results of recomputing the near field with a radial sampling rate of $6 \times f/c$. Note the improvement in the accuracy of this result versus that of Fig. 6(c).

To compute the axial pressure field results of Fig. 6 (a)–(d) the source plane, normal velocity description had to be propagated with a normal velocity to pressure point spread function. The function used was[5]

$$h_{\text{up}}(z,r) = -if\rho(e^{ik\sqrt{z^2+r^2}}/\sqrt{z^2+r^2}). \quad (8)$$

This function can be used directly in the SSC propagation step or its analytical transform could be used with the RFSC step.

An alternative route to obtain pressure field results based on a source normal velocity description is to convert the initial (planar) normal velocity description to an initial (planar) pressure description. The conversion of the source plane description from normal velocity to pressure (or vice versa) can be performed using the expression[12]

$$p(0,r) = \rho c F^{-1}[\mathbf{F}[u(0,r)]k/k_z], \quad (9)$$

where $p(0,r)$ is the source plane pressure profile, $u(0,r)$ is the source plane normal velocity profile, and

$$k_z = [k^2 - (2\pi R)^2]^{1/2}, \quad |R| \leqslant f/c$$
$$= i[(2\pi R)^2 - k^2]^{1/2}, \quad |R| > f/c.$$

An important point to be noted here is that associated with a finite acoustic normal velocity profile, is an infinite extent pressure profile. Thus, the use of Eq. (9) to compute the source pressure profile with the DHT can be problematic due to the presence of convolutional wraparound errors. These errors appear to be insignificant only when the transform extent T is an integer multiple of the propagating wavelength. The source plane pressure field could be propagated using the same algorithms and h and H functions [(3) and
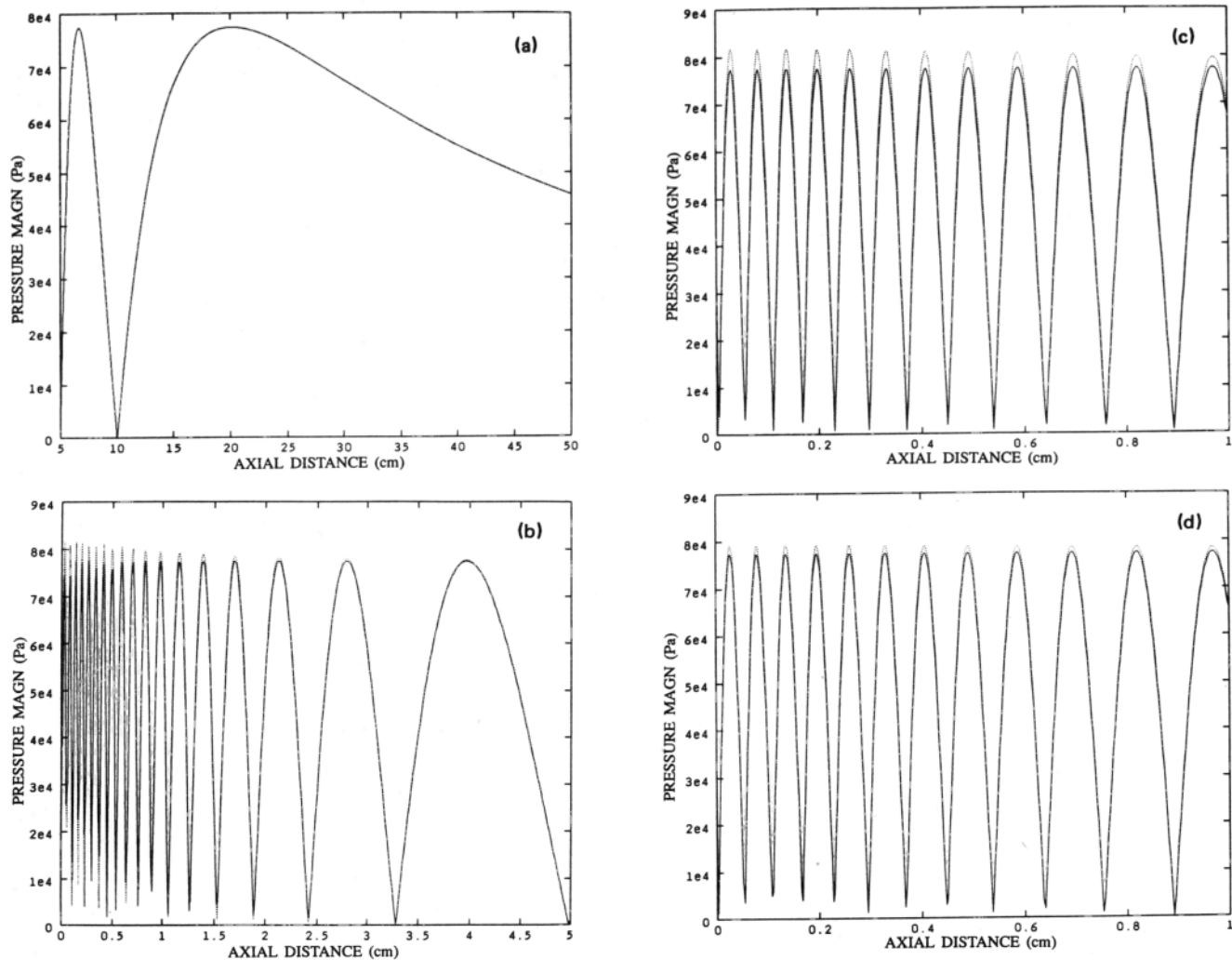
FIG. 6. On-axis sound pressure magnitude versus axial distance for the 3-MHz uniform piston source. The analytical solution results (solid curves) are given along with the DHT-based, SSC multistep algorithm results (dotted curves). Note the exponential notation on the pressure axis. (a)–(c) different axial ranges showing results obtained with the SSC multistep algorithm using $N = 240$ and $T = 3$ cm (thus sampling at $2 \times f/c$). In (a) the two results show no visible differences. The multistep result is erroneously high in the near field (b)–(c), though. (d) near-field axial results over the same range as (c), but here using $N = 360$ and thereby sampling at $3 \times f/c$. Note the considerable improvement in agreement between the multistep SSC result and the analytical result.

(4)] as with the propagation of a source plane normal velocity field. The results will not be as accurate though, as the corresponding propagation of the normal velocity source description, since the source pressure description is necessarily a truncated version of the real source plane pressure profile.

Applying the SSC- and RFSC-based, multistep algorithms to an initial normal velocity, planar description of this source reveals an interesting difference between acoustic particle velocity and acoustic pressure in the nearfield of a uniform piston source. Figure 7(a)–(e) shows overlays of the radial and axial, pressure and normal velocity amplitude curves for the same unfocused piston transducer. The axial pressure curves were calculated using the analytical expression (7). The normal velocity curves have been scaled up by the factor ρc. The radial curves in Fig. 7(a) are from $z = 1\lambda$. Note the initial differences, and eventual convergence, of the axial curves. The initial differences between the cures reflects the failure of the plane wave impedance relation $p = \rho c u$ in describing the nearfield of an unfocused piston

source. The results of Fig. 7(a)–(c) were obtained using the SSC-based algorithm. The small wiggle in the RFSC-based results of Fig. 7(d) and (e) is an artifact of the frequency sampling performed—still present, though greatly reduced, from the original FSC formulation. The wiggle can be indefinitely reduced by increasing T (and thus the spatial frequency resolution).

A more continuous multistep, propagation algorithm based on the SSC (or RFSC) step would return each of the planar fields computed (except the last) back to the source plane and then restart the SSC (or RFSC) step using the returned field. This can be easily accomplished by deconvolving the field at each plane with the same $h_d(i)$ samples that were used in convolving the source field to that plane (since $U_d = S_d \times H_d$, then $S_d = U_d / H_d$). This multistep scheme we call the "back-and-forth" approach. In general, this is computationally redundant and thus undesirable, but in the case of the nonlinear propagation of a field, in which nonlinear effects can be added as a separate step between
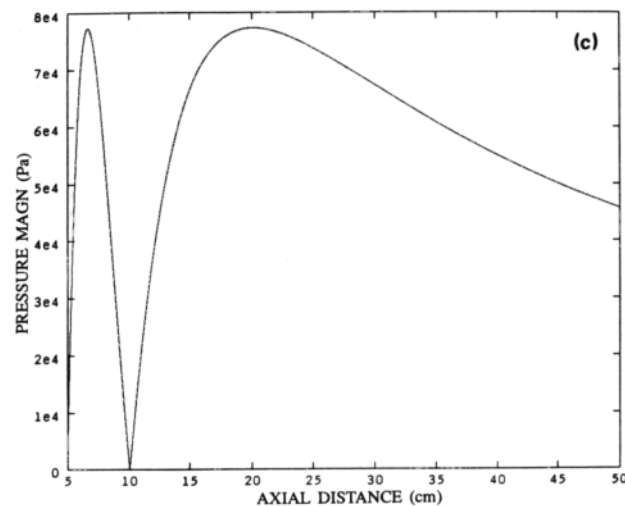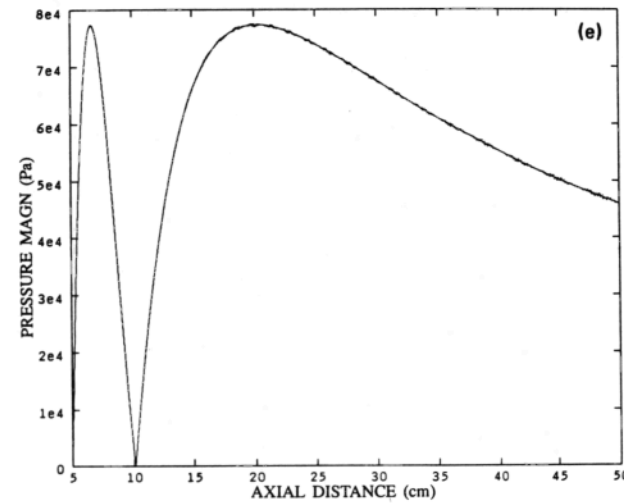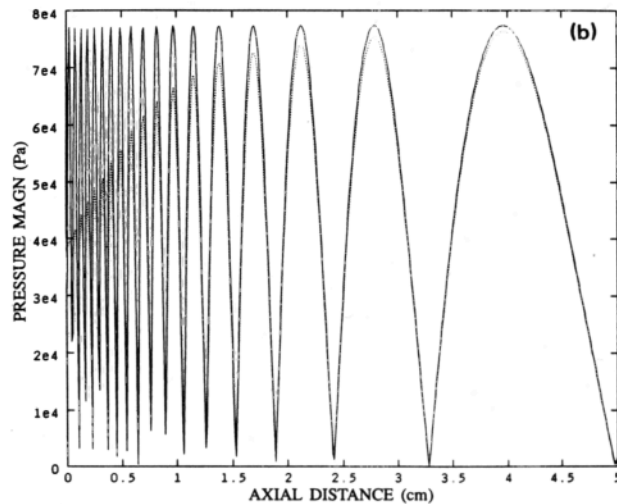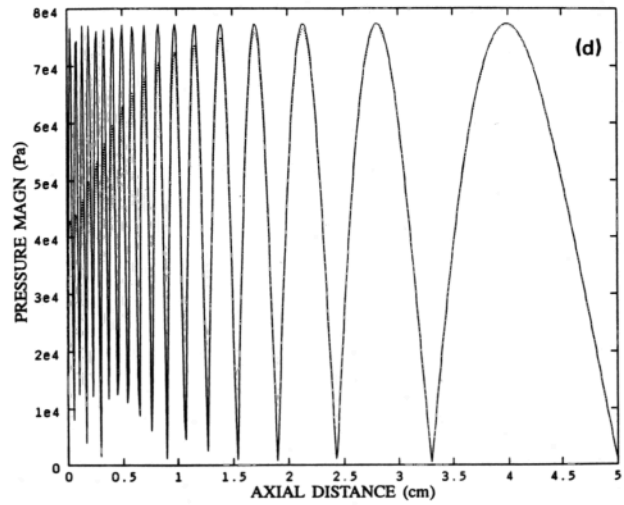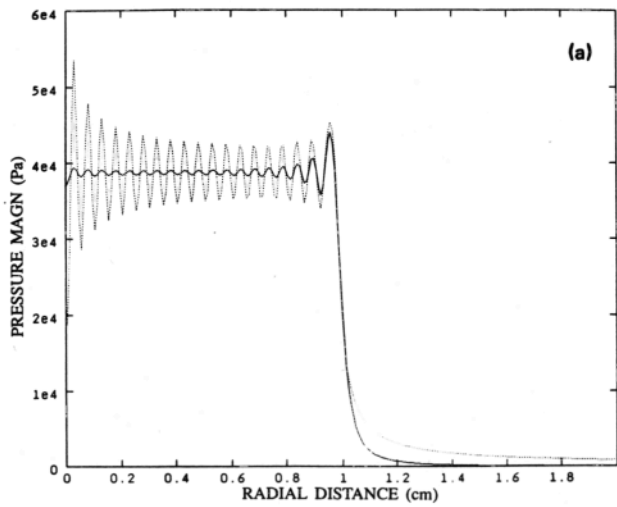
FIG. 7. Normal velocity $\times \rho c$ magnitude versus pressure magnitude for the 3-MHz uniform piston source. Note the exponential notation on the pressure axis. (a) $z = 1\lambda$ radial results for normal velocity $\times \rho c$ (solid curve) and pressure (dotted). (b)–(c) near and far field, axial normal velocity $\times \rho c$ computed using the SSC multistep algorithm (dotted curves). The solid curve is the analytically derived pressure magnitude. Note the gradual convergence of the curves in the near field. (d)–(e) identical to (b)–(c) except that the normal velocity $\times \rho c$ curves were obtained using the constant step size, RFSC multistep algorithm.

subsequent planes, it is essential that the nonlinear transfer of energy amongst the various harmonic fields be maintained by the multistep diffraction algorithm. In this case, the deconvolution back to the source plane can be viewed as providing a nonlinear update to the "effective" multiharmonic source.

A very simple, multistep scheme can be devised using the RFSC step when the multiple output planes are separat-

ed by a constant Δz increment. For the first step follow the RFSC single step approach. Each subsequent Δz propagation step is completed by multiplying the current field's (*not* the source's) DHT by a trimmed version of the first step's $\widehat{H}_d^{\Delta_z}(m)$ samples. The incremental trimming or truncating of the $\widehat{H}_d^{\Delta_z}(m)$ function is performed to avoid wraparound errors of the field in the subsequent plane as prescribed by expression (6). For values of T equal to the axial extent of

P. T. Christopher and K. J. Parker: Linear propagation

propagation, this algorithm gives accurate multistep field propagation results. It is also extremely fast as it requires the computation of only one set of $\hat{H}_d^{\Delta_z}(m)$ $m = 1,...,m_{max}$ values, as opposed to one set of $h_d(i)$, $i = 1,...,N-1$ values (where $R_{m_{max}} \approx f/c$ and $m_{max} \ll N-1$) and their DHT *per step* in the SSC multistep approaches. Note, this constant step size RFSC scheme gives results identical to that of the straightforward approach of repeating the RFSC step from the source to each plane, however the constant step size RFSC approach saves significant computer time by using one set of $\hat{H}_d$ values which are truncated as required. This algorithm is also adequate for the propagation needs of multistep, nonlinear propagation.

The computer time required to calculate the results of Fig. 7 reveals the savings possible through use of the RFSC propagation scheme. The axial results of Fig. 7(b)–(e) involved the advancement of the field through 2750 Δz increments. The SSC-based results of 7(b) and (c) required 2 hours on a VAXstation II/GPX, while the corresponding constant step size RFSC-based results of 7(d) and (e) required only 4 min. Thus, if the small artifacts of the RFSC approach are acceptable, then the speed of the RFSC multistep algorithm can be a great convenience, in particular in the case of the repetitive use of one or more Δz step sizes.

V. INCLUSION OF FREQUENCY-DEPENDENT MEDIUM ATTENUATION

Frequency dependent losses in the medium can be added to either the SSC or the RFSC propagation approaches. Medium attenuation is here modeled for spherical or plane waves by the expression

$$\exp(-\alpha f^n \cdot d), \tag{10}$$

where d is the distance propagated in the medium[13] and a power law relation for attenuation versus frequency is assumed. This expression is appropriate for weak attenuation in which $\alpha/k \ll 1$.[11] For stronger attenuation, a complex (dispersive) expression such as the one derived in Ref. 11 could be used instead of (10). Expression (10) can be appended to the $h(z,r)$ point normal velocity (or pressure) spread function to form an attenuated point spread function

$$h_a(z,r) = h(z,r) \times \exp(-\alpha f^n \cdot \sqrt{z^2 + r^2}). \tag{11}$$

This attenuated function can then be used in place of h in any algorithm using the SSC step.

Attenuation can be added in the spatial frequency domain to the function $H(z,R)$ in order to account for medium attenuation in the RFSC propagation step. The resulting updated function is

$$H_a(z,R) = H(z,R)$$
$$\times \exp(-\alpha f^n \cdot \{z/\cos[\sin^{-1}(Rc/f)]\}), \tag{12}$$

where the expression in place of d on the right accounts for the distance traveled by the plane wave component specified by spatial frequency R in the angular spectrum interpretation as stated in Eq. (5).

There is one notable difference between the attenuation computed using $h_a(z,r)$ and that computed using $H_a(z,R)$.

In using the RFSC scheme, in which evanescent waves are always neglected, $H_a(z,R)$ correctly only applies the attenuation of (10) to the propagating or plane wave components of the source. In using the SSC scheme, in which evanescent waves are never neglected [however small they might be, they are always included in the $h(z,r)$ expression], $h_a(z,r)$ incorrectly applies (10) to both the evanescent and propagating components of the source's field. Thus, when propagating over very short distances ($<\lambda$) and facing very large attenuation (significant over distances $<\lambda$), the SSC-h_a propagation scheme will give erroneous results reflecting its use of (10) on the evanescent components.

To check the equivalence of the two attenuation schemes, Fig. 8(a) displays an overlay of the Rayleigh distance radial field results obtained by using an attenuated SSC step [with $h_a(z,r)$] and an attenuated RFSC step [with $H_a(z,R)$] for the previously described 3-MHz unfocused piston source. The propagation parameters used for the SSC and RFSC steps are identical to those used in Fig. 5, except
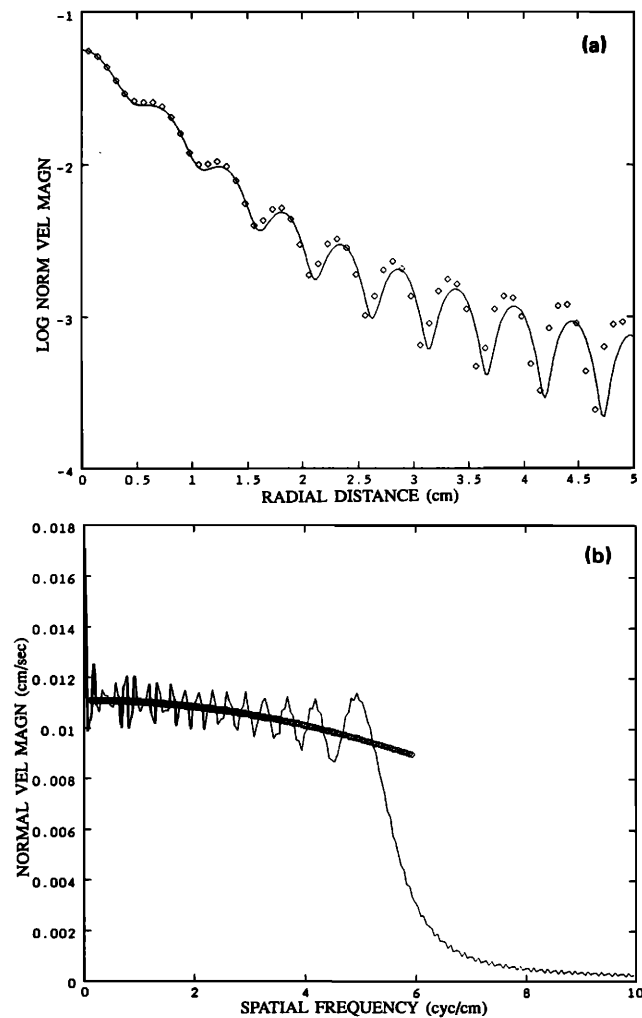

FIG. 8. Comparison of the spatial and spatial frequency domain attenuation algorithms. (a) Rayleigh distance (20-cm) radial field results for the 3-MHz uniform piston in a heavily attenuating medium using the SSC (solid curve) and RFSC ($\Diamond$'s) attenuated steps. Note the agreement (except for the scaling) between these results and those shown for the unattenuated propagation in Fig. 5(c). (b) the SSC H_d function (solid) and RFSC $\hat{H}_d$ function ($\Diamond$'s).

that the medium attenuation used in this example was $\alpha = 0.025$ and $n = 2$ which is approximately 100 times the measured attenuation of water. Figure 8(b) shows an overlay of the SSC step's H_d and the RFSC step's $\hat{H}_d$ curves. Note the increasing influence of attenuation at bigger values of R which corresponds to larger d's or equivalently larger θ's (for the plane wave components representing h).

VI. MULTILAYER PROPAGATION

To extend the capabilities of the multistep SSC and RFSC approaches to include propagation through multiple, parallel layers of fluid medium (without the inclusion of multiple reflections between the boundaries, that are not relevant to the authors' biomedical applications), Snell's law and the transmission coefficient must be accounted for. Fortunately, Snell's law is implicit in the h and H propagation scheme. To see this, consider a plane wave travelling in medium A with a direction that forms an angle θ_{in} with the norm of the boundary plane with medium B. By Eq. (5) this implies a spatial frequency $R_{\text{in}} = (f/c_A)\sin \theta_{\text{in}}$ in the boundary plane. Continuity of the normal component of acoustic velocity implies continuity of the phase of this component, and thus $R_{\text{tr}} = R_{\text{in}}$. This relationship is always maintained in the h and H scheme since the spatial frequency of any component is always preserved. Substituting from the geometric spatial frequency relation (5) gives the desired Snell's law

$$\sin \theta_{\text{in}} / \sin \theta_{\text{out}} = c_A/c_B. \tag{13}$$

Using the SSC or RFSC approaches without modification to cross a fluid boundary would not account for the reflected field and thus fails to conserve energy and momentum. Stated differently, the amplitude of the transmitted plane waves does not agree with those given by the complex analytical transmission coefficients[11]

$$T^p = 2\left(\frac{\rho_A c_A}{\rho_B c_B} \times \frac{\cos\theta_{\text{out}}}{\cos\theta_{\text{in}}} + 1\right)^{-1},$$
$$T^u = T^p \times (\rho_A c_A / \rho_B c_B), \tag{14}$$

where T^p and T^u are the pressure and velocity transmission coefficients, respectively, and θ_{in} and θ_{out} are complex to account for evanescent waves.

A multilayer point spread function h^m which would account for all propagation effects through multiple fluid layers does not appear to be analytically derivable or easily numerically approximated. Thus, updating the SSC approach to allow for multiple layers appears to be very difficult. One problem is that in the spatial domain evanescent energy is not separated from nonevanescent energy, and thus couldn't be properly transmitted using (14). Even neglecting the evanescent waves, an explicit analytical expression for h^m appears unlikely, and further each $h^m(z,r)$ value appears to require an involved numerical estimate.

Boundary crossing in the spatial frequency domain appears to be much easier. H is an explicit function of R and thus θ. One simple spatial frequency domain algorithm consists of a straightforward combination of the transmission coefficients of (14) and the RFSC propagation step. An analytical, multiple layer H^m function can be written as

$$H^m(z,R) = H_A(\Delta z_A, R) \times T^u_{AB}(R) \times H_B(\Delta z_B, R) \times \cdots$$
$$\times T^u_{IJ}(R) \times H_J(\Delta z_J, R), \tag{15}$$

where

$$T^u_{AB}(R) = 2\frac{\cos[\theta_{\text{out}}(R)]}{\cos[\theta_{\text{in}}(R)]}\left(\frac{\cos[\theta_{\text{out}}(R)]}{\cos[\theta_{\text{in}}(R)]} + \frac{\rho_B c_B}{\rho_A c_A}\right)^{-1}$$

is the complex, velocity transmission coefficient for the boundary between medium A and medium B [expression (13) allows this to be converted to the corresponding pressure transmission coefficient]. θ_{in} and θ_{out} express θ as function of R via (5) and $z = \Delta z_A + \Delta z_B + ...\Delta z_J$. Also note the difference between T^u_{AB} and T^u as given by (13) is due to the implicit transmission coefficient already present in $H^A \times H^B$ [the fact that $H^A \times H^B$ has a nonunity transmission coefficient that must be corrected for before applying (14), is apparently commonly neglected]. To examine the propagation of evanescent waves in the vicinity of a boundary, expression (15) can be integrated numerically to obtain an appropriate set of h^m samples, or placed in the analytical convolution integral and then numerically integrated. The numerical integration could utilize variable step sizes to avoid problems with the rapid phase changes of H as $R \rightarrow f/c$.

Here H^m can be sampled and utilized as in the RFSC algorithm. The only complication is keeping track of the maximum spatial frequency component allowable in a given plane (which doesn't wraparound the spatial aperture T). This is trivial in the spatial frequency domain (tag each spatial frequency component with its greatest possible radial extent at the current plane, update and check these tags with each Δz advancement)—unlike with h_m in the spatial domain. Results from an example using this algorithm are shown in Fig. 9(a) and (b). Consider the field of a 3-MHz focused piston transducer operating in water and operating in a two-layer medium of fat and liver. The water medium has parameters $c = 1500$ m/s, $\rho = 1.0$ g/cm^3, $\alpha = 0.00025$ Np/cm MHz, and $n = 2$. The two-layer medium consists of 2 cm of fat with parameters $c = 1460$ m/s, $\rho = 0.95$ g/cm^3, $\alpha = 0.15$ Np/cm MHz, and $n = 1.0$, followed by 10 cm of liver with parameters $c = 1570$ m/s, $\rho = 1.05$ g/cm^3, $\alpha = 0.03$ Np/cm MHz, and $n = 1.3$.[13,14] The initial source peak acoustic intensity is 0.1 W/cm^2 and the transducer radius is 1 cm. The geometric focal length (F) is 10 cm. The focusing was accomplished by applying a spherically focusing phase factor $[e^{j\theta(r)}$, where $\theta(r) = (2\pi f/c)\sqrt{r^2 + F^2}]$ to the source plane amplitude profile. The computed axial and radial (at $z = 10$ cm) normal velocity fields are shown in Fig. 9(a) and (b). The computer runs for both mediums (water and fat/liver) involved 600 Δz advancements of the acoustic particle velocity fields and took only 50 s using the constant step size RFSC approach on the authors' VAXstation II/GPX.

The results of Fig. 9 depict dramatically the effects of the high attenuation of the biomedical imaging, fat and liver layered medium. The axial velocity magnitudes in the fat-/liver medium are much lower than in the corresponding water propagation. Also the axial maximum magnitude occurs earlier in the layered medium in part due to the increased attenuation. The effects of the boundary crossing are
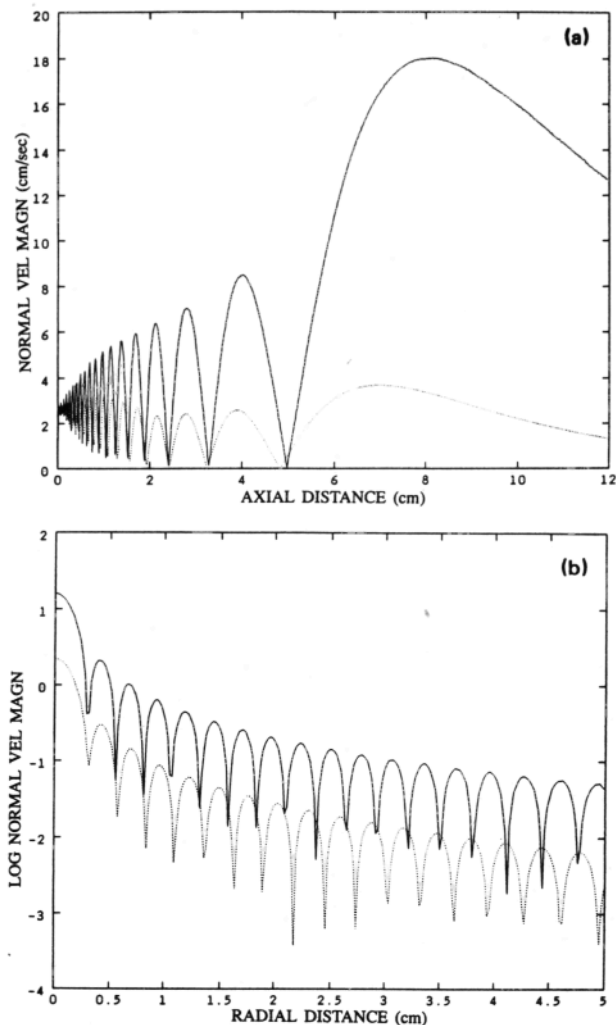
FIG. 9. Multilayer RFSC propagation example. A 3-MHz focused piston transducer is propagated through water and compared to propagation through a two layer medium. The geometric focal length of the transducer is 10 cm and its radius is 1 cm. The two-layer medium consists of 2 cm of fat followed by 10 cm of liver. (a) Axial particle velocity magnitudes for water (solid curve) and the fat/liver medium (dotted). (b) The log of the corresponding focal plane ($z = 10$ cm) radial results.

more subtle due to the closeness of the two medium's parameters. In the radial plot of Fig. 9(b) the layered medium's sidelobes show a gradual shift away from the axis at increasing radial distance, relative to the corresponding sidelobes of the water propagation. This agrees with the Snell's law phenomenon of rays shifting away from the norm when passing from a slow medium (fat) into a faster one (liver). This same phenomenon should cause the focus in the layered medium to occur earlier (prematurely). This is visible in earlier occurrence of the last axial minimum.

VII. CONCLUSIONS

A number of new approaches to the linear propagation of diffractive fields have been presented. A discrete Hankel transform is used to efficiently propagate radially symmetric fields. The sampling of the spatial domain point spread function is shown to be more accurate and reliable than the common approach of sampling its transform. Extensions to multistep propagations are given including the effects of attenuation and transmission coefficients in layered media. The results form an efficient computational tool for acoustic field propagation. The methodology will be applied to nonlinear diffractive field propagation in a companion paper. Currently under development are efficient extensions of these methodologies to handle nonradially symmetric sources, nonsinusoidal sources, and nonplanar sources.

ACKNOWLEDGMENTS

[1] J. D. Gaskill, *Linear Systems, Fourier Transforms, and Optics* (Wiley, New York, 1978).
[2] J. A. Ratcliffe, "Some aspects of diffraction theory and their applications to the ionsphere," Rep. Prog. Phys. **19**, 188–263 (1956).
[3] J. A. Goodman, *Introduction to Fourier Optics* (McGraw-Hill, New York, 1968).
[4] E. G. Williams, and J. D. Maynard, "Holographic imaging without the wavelength resolution limit," Phys. Rev. Lett. **45**, 544–557 (1980).
[5] E. G. Williams and J. D. Maynard, "Numerical evaluation of the Rayleigh integral for planar radiators using the FFT," J. Acoust. Soc. Am. **72**, 2020–2030 (1982).
[6] P. R. Stepanishen and K. C. Benjamin, "Forward and backward projection of acoustic fields using FFT methods," J. Acoust. Soc. Am. **71**, 803–812 (1982).
[7] R. C. Waag, J. A. Campbell, J. Ridder and P. R. Mesdag, "Cross-sectional measurements and extrapolations of ultrasonic fields," IEEE Trans. Sonics Ultrason. **SU-32**, 26–35 (1985).
[8] M. E. Schafer and P. A. Lewin, "Transducer characterization using the angular spectrum method," J. Acoust. Soc. Am. **85**, 2202–2214 (1989).
[9] H. F. Johnson, "An improved method for computing a discrete hankel transform," Comp. Phys. Comm. **43**, 181–202 (1987).
[10] A. V. Oppenheim and R. W. Schafer, *Digital Signal Processing* (Prentice-Hall, Englewood Cliffs, NJ, 1975).
[11] L. E. Kinsler, A. R. Frey, A. B. Coppens, and J. V. Sanders, *Fundamentals of Acoustics* (Wiley, New York, 1982).
[12] E. G. Williams, "Numerical evaluation of the radiation from unbaffled, finite plates using the FFT," J. Acoust. Soc. Am. **74**, 343–347 (1983).
[13] M. E. Lyons and K. J. Parker, "Absorption and attenuation in soft tissues II—experimental results," IEEE Trans. Ultrason. Ferr. Freq. Cont. **35**(4), 511–521.
[14] S. A. Goss, R. L. Johnson, and F. Dunn, "Compilation of empirical ultrasonic properties of mammalian tissues. II," J. Acoust. Soc. Am. **68**, 93–108 (1980).